Photoacoustic elastography based on laser-excited shear wave

Yang Liu [*,†,§], Ruoyi Shi [†,§], Gang Li [*,†] and Mingjian Sun [*,†,‡]

*School of Astronautics, Harbin Institute of Technology
Harbin 150000, P. R. China

†School of Information Science and Engineering
Harbin Institute of Technology, Weihai 264200, P. R. China
‡sunmingjian@hit.edu.cn

Elastography can be used as a diagnostic method for quantitative characterization of tissue hardness information and thus, differential changes in pathophysiological states of tissues. In this study, we propose a new method for shear wave elastography (SWE) based on laser-excited shear wave, called photoacoustic shear wave elastography (PASWE), which combines photoacoustic (PA) technology with ultrafast ultrasound imaging. By using a focused laser to excite shear waves and ultrafast ultrasonic imaging for detection, high-frequency excitation of shear waves and noncontact elastic imaging can be realized. The laser can stimulate the tissue with the light absorption characteristic to produce the thermal expansion, thus producing the shear wave. The frequency of shear wave induced by laser is higher and the frequency band is wider. By tracking the propagation of shear wave, Young's modulus of tissue is reconstructed in the whole shear wave propagation region to further evaluate the elastic information of tissue. The feasibility of the method is verified by experiments. Compared with the experimental results of supersonic shear imaging (SSI), it is proved that the method can be used for quantitative elastic imaging of the phantoms. In addition, compared with the SSI method, this method can realize the noncontact excitation of the shear wave, and the frequency of the shear wave excited by the laser is higher than that of the acoustic radiation force (ARF), so the spatial resolution is higher. Compared to the traditional PA elastic imaging method, this method can obtain a larger imaging depth under the premise of ensuring the imaging resolution, and it has potential application value in the clinical diagnosis of diseases requiring noncontact quantitative elasticity.

Keywords: Elastography; shear wave; photoacoustic; Young's modulus.

---

‡Corresponding author.
§These authors contributed equally to this work.

1. Introduction

Any biological tissue has viscosity and elasticity, and when biological tissue is diseased, its elastic properties change significantly. Thus, the elastic properties of tissues can be used as important indicators for disease diagnosis.[1–3] As a diagnostic method to quantitatively characterize the information about tissue elasticity, elastography has been widely used in clinical diagnosis.[4–6]

Shear wave elastography (SWE) is a rapidly developing elastography technique in recent years.[7,8] Shear wave excitation methods currently used in elastography mainly include acoustic radiation force (ARF) pulse excitation and external mechanical vibration. Supersonic shear imaging (SSI), which was first proposed by Bercoff *et al.* in 2004, uses ARF as the excitation source of the shear wave.[9] Transient elastography (TE) uses external vibrators to generate low-frequency vibrations to excite shear waves.[10] These excitation methods cannot achieve noncontact excitation of shear waves, which has limitations in application. It has been found that a short-pulse laser can stimulate tissue to generate large-bandwidth surface acoustic waves (SAW) and shear waves in a noncontact manner.[11,12] However, laser excitation shear wave has not yet been applied to the field of quantifying the elasticity of biological tissues.

Laser-induced shear waves are essentially ultrasonic waves generated by the interaction between lasers and soft tissues when a laser irradiates soft tissues, which is a photoacoustic (PA) signal.[13] With the development of PA imaging techniques, elastography methods that combine PA technology have been proposed.[14–16] The main technical methods are divided into three categories: analyzing the viscoelasticity of the tissue using PA signal relaxation characteristics,[17] quantifying elasticity using the PA phase resolution method[18] and quantitative elasticity based on the correlation of the PA signal of the tissue before and after compression, more specifically, vibration or displacement.[19,20] These techniques utilize the PA signal of the tissue being examined, which is dependent on the absorption of light by chromophores within the tissue. For tissues with strong surface light absorption, the penetration depth is limited, making it challenging to obtain clear images of deeper structures, such as organs located in the chest or abdomen, without compromising the signal-to-noise ratio (SNR) and/ or spatial resolution.[35] The elastic properties can be obtained noninvasively by obtaining a tissue model from a laser-induced PA initial pressure wave. This will improve the potential applications of PA imaging and extend it to the diagnosis and treatment of diseases such as cancer and brain tumors, which can result in significant contrast to the elastic properties of normal tissues.[35–37]

In this study, we propose a novel linear array SWE method that combines laser-excited shear wave technology with ultrafast ultrasound imaging, called photoacoustic shear wave elastography (PASWE). This method can realize noncontact shear wave excitation. The shear wave excited by the laser has higher frequencies and wider bandwidths than those excited by the ARF, which is more conducive to obtaining high-resolution elastic images. Furthermore, this method overcomes the limitations of existing PA elastography methods in terms of penetration depth. We first verified the internal mechanism of laser-excited shear waves. Then, homogeneous and heterogeneous phantoms were made for the experiments, and the PASWE experimental results were compared with the results of SSI and actual Young's modulus values to verify the feasibility and accuracy of the method proposed in this paper.

2. Materials and Methods

2.1. *Principle of PASWE*

Since shear waves belong to a kind of ultrasound wave excited by laser irradiation of biological tissues, laser excitation of shear waves belongs to the process of laser-induced ultrasound. According to the energy density of the incident laser and the material damage threshold, there are two main mechanisms by which lasers excite ultrasonic signals: the thermoelastic mechanism and the thermal cauterization mechanism.[21,22] When the incident laser energy density is higher than the surface damage threshold of the material, a stronger shear wave will be generated, and the estimation of the elastic modulus will be more accurate, but this method will cause irreversible damage to the tissue and does not meet the requirements of clinical medical diagnosis. Therefore, we must strictly control the energy density of the laser to avoid tissue damage. In this paper, we discuss only the excitation of shear waves under the thermoelastic mechanism. In subsequent experiments, the laser
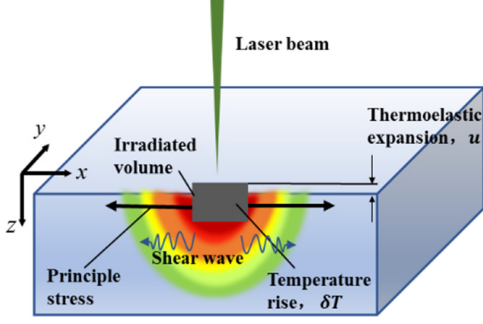
Fig. 1. Schematic diagram of the laser excitation shear wave principle under thermo-elastic mechanisms.

energy will be strictly controlled within the tissue damage threshold.

Figure 1 shows the schematic diagram of the laser excitation shear wave principle under the thermoelastic mechanism. When a short-pulse laser beam hits biological tissue, the light absorber in the biological soft tissue absorbs part of the energy of the incident laser and converts it into heat energy, causing a local temperature rise.

Small displacement occurs in the z-axis direction, and the propagation of displacement appears as shear waves propagating outward. The strain caused by temperature rise $\delta T(z,t)$ satisfies the following equation[23]:

$$\varepsilon_z = \frac{\partial u(z,t)}{\partial z} = \alpha \delta T(z,t), \tag{1}$$

where u is the displacement component of particle vibration in the z axis direction and α is the linear expansion coefficient. When the part of the sample is irradiated by the laser and the temperature rises, the rest will generate lateral constraints. In this case, according to the thermoelastic theory, u satisfies the following equation[24]:

$$\rho \frac{\partial^2 u}{\partial t^2} = (\lambda + 2\mu)\frac{\partial^2 u}{\partial z^2} - 3(\lambda + \frac{2}{3}\mu)\alpha \frac{\partial T(z,t)}{\partial z}. \tag{2}$$

Due to the presence of transverse constraints, the expansions occur in the axial direction. The process of axial displacement change is the process of shear wave propagation. The group velocity c_s of the shear wave is proportional to the shear modulus μ of the medium, as shown in the following equation[25]:

$$\mu = \rho c_s^2, \tag{3}$$

where ρ is the density of the elastic material. The density ρ of soft tissue is usually assumed to be

$1000 \, \text{kg/m}^3$.[26] The relationship between the elastic modulus E and the shear modulus μ satisfies the following equation[27]:

$$E = 2\mu(1 + v), \tag{4}$$

where v is Poisson's ratio of the material. For biological soft tissues, it is generally believed that soft tissue cannot be compressed, that is, v is approximately equal to 0.5.[19,20] Therefore, the relationship between shear wave velocity c_s and elastic modulus (Young's modulus) E can be deduced, as shown in the following equation:.

$$E = 3\rho c_s^2. \tag{5}$$

2.2. *Experimental setup and data process*

Figure 2 illustrates the setup of the experiment. A pulse laser (SpitLight, Innolas, Germany) operating at 532 nm with a repetition rate of 20 Hz, a pulse width of 7 ns, was used as an excitation source. The laser flux $(10 \, \text{mJ/cm}^2)$ we used in our experiment is within the safety limits of the American National Standards Institute. The laser beam emitted by the pulsed laser was focused on the sample through a focusing mirror. A commercial ultrasound scanner (Prodigy, S-Sharp, Taipei, China) equipped with an ultrafast ultrasound imaging function is connected to a linear array ultrasound transducer (L7.5-12840C, S-Sharp, Taipei, China), which consists of 128 array elements and a center frequency of 7.5 MHz, to detect small displacement caused by shear wave propagation in a short period of time. In the experiment, the sampling frequency was 20 MHz. In addition, the prodigy system can implement SSI, which can be used to provide data analysis comparison.

During our experiment, the laser beam hits from one side of the sample and the ultrasonic transducer receives echo signals on the other side. The imaging plane of the ultrasonic transducer and the laser optical path are kept at the same level. To enable shear wave excitation and detection beam emission at the same time, the output signal of the pulsed laser is connected to the ultrasound scanner through a cable as a trigger signal for data acquisition. Immediately after laser emission, the ultrasonic transducer is triggered to emit plane waves at three angles $(-2°, 0°, 2°)$ to acquire two-dimensional (2D) ultrasound data of the tissue of successive frames during shear wave propagation. We use
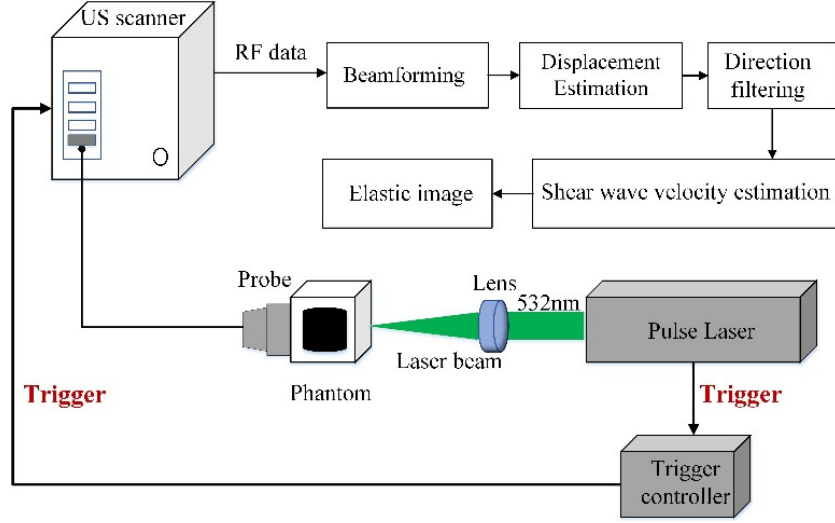
Fig. 2. Schematic diagram of the experimental system.

plane waves to track shear waves, and after the plane waves are transmitted, all channels of the ultrasonic probe receive them, so as to improve the resolution and accuracy of the signal and increase the reliability of detection. The parameter PRF is a composite pulse signal composed of multiple plane waves, and the pulse repetition frequency is set to 5 kHz. Each plane wave emits 32 pulses and obtains 32 sets of ultrasonic echo data. The signal output from the ultrasound scanner is the baseband signal obtained by demodulating the radio frequency (RF) signal. The baseband signal is processed offline to calculate the elastic modulus of the tissue. First, the data from the three plane waves are compounded to improve the SNR. When shear wave propagates, the deformation of the structure in the axial direction will result in the phase shift of the two adjacent ultrasonic echo signals. The ultrasonic echo signal obtained at different times has a certain phase delay, which is caused by the change of tissue displacement. In order to analyze the change of tissue displacement with time, we send three plane waves at different angles to track the shear wave. The (1D) autocorrelation algorithm is used to calculate the phase difference of the signals at the same scanning position of every two consecutive pulse echo signals.[28] The z-axis direction displacement $d(t)$ of the sample at moment t can be calculated using the following equation[30,31]:

$$d(t) = c\frac{\theta(t)}{2\pi f_0},\qquad(6)$$

where $\theta(t)$ is the phase difference of two pulse echoes at the same scanning position at time t and moment

$t - 1$. f_0 is the center frequency of the probe. c is the speed of sound. Then, the z-axis direction displacement of each pixel of the scanning position in different frames is obtained. The direction filtering algorithm separates forward and backward propagating shear waves to avoid interference from shear wave reflection and refraction on the wave velocity estimation results.[29,30] Based on the filtered displacement data, the shear wave velocity is estimated using the time-of-flight (TOF) algorithm.[31] According to Eq. (5), the modulus of elasticity can be further obtained. For viscoelastic tissues, the K-space algorithm can be used to analyze shear wave velocities (phase velocities) at different frequencies. Perform a 2D Fourier transform on the spatial-temporal data on sample displacement of the selected Region of Interest (ROI) to obtain a K-space displacement map. According to the K-space displacement data, the phase velocity at that time frequency can be obtained by dividing the time frequency by the number of waves of the maximum energy peak at that time frequency.

In addition, the SNR of elastic image is introduced to evaluate the variance of elastic modulus estimation. The definition of SNR is as follows:

$$\mathrm{SNR} = 20\lg\left(\frac{\mu_e}{\sigma}\right),\qquad(7)$$

where μ_e is the average elastic modulus in the elastic uniform region. σ is the variance of the elastic modulus in this region.

For heterogeneous experiments, the contrast-to-noise ratio (CNR) of elastic images is introduced

to evaluate the possibility of detecting hard blocks in elastic images.

$$\text{CNR} = 20\lg\frac{|\mu_H - \mu_B|}{\sqrt{\sigma_H^2 + \sigma_B^2}}, \qquad (8)$$

where μ_H and μ_B are the average shear wave velocity of content and background, σ_H and σ_B are the variance of shear wave velocity in content and background, respectively.

3. Results

3.1. *Laser-excited shear wave PA elastography verification*

In order to verify whether the ability of laser to excite shear waves depends on the light absorber in the medium, we first conducted a comparative experiment, using a gelatin-based phantom as the experimental sample. The schematic diagram of the phantom is shown in Fig. 3. The background of the phantom was composed of 5% gelatin and 0.5% resin, and the inclusion was a hard block composed of 10% gelatin and 12% graphite. Resin and graphite were added to provide sound scattering, and the graphite also increased the light absorption. As shown in Fig. 3, the laser beam was vertically focused in positions A, B, and C, and the ultrasonic transducer was placed on the other side of the phantom to perform data acquisition.

After one-dimensional (1D) autocorrelation processing of the acquired data, the displacement image of successive frames of the phantom was
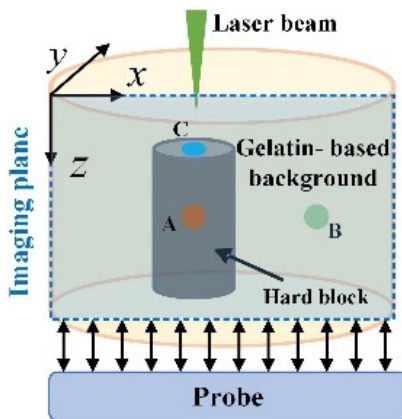

Fig. 3. Schematic diagram of the phantom and laser beam setup.

obtained. Figure 4 shows the displacement maps at 1, 3.5, 6, and 8.5 ms after laser excitation at points A, B, and C, respectively. It can be clearly seen that in Figs. 4(a) and 4(c), the shear wave propagates outward with time. In Fig. 4, it is obvious that the waves propagate in both directions, red represents the peak, blue represents the trough, and the speed at which the wave-front propagates is the shear wave velocity. The position where the shear wave is generated is inside the model, which coincides with the position of the light absorber. In Fig. 4(b), there is no shear wave generation. Therefore, it can be proved that the shear wave generation in the case of laser focusing is related to the light absorber at the focus position.

3.2. *Homogeneous phantom experiments*

It was previously verified that the laser can excite shear waves in Sec. 3.1. In this section, we made a homogeneous phantom (Fig. 5) composed of 10 g gelatin 10 g graphite and 80 g water to carry out the PASWE experiment to verify the ability of the proposed method to quantify elasticity.

The displacement maps of 1.5, 3, 4.5, and 6 ms after laser excitation were obtained after 1D autocorrelation processing (Fig. 6(a)). Figure 6(b) shows the spatial-temporal map of displacement, where the white line approximates the trajectory of the wave peak, and its slope is the group velocity of the shear waves. The spatial-temporal data was converted into K-space by a 2D Fourier transform, where K-space represents the frequency-wave number spectrum of tissue displacement as shown in Fig. 6(c).

In K-space, the horizontal axis represents the frequency and the vertical axis represents the wavenumber. The phase velocity of the shear wave was obtained by ω/k, where ω is the frequency and k is the wave number. The shear wave phase velocity and the group velocity of the homogeneous phantom are similar. The average phase velocity shown in Fig. 6(d) is 4.86 m/s, which is very close to the phase velocity determined by the group velocity shown in Fig. 6(b) (4.89 m/s).

The TOF algorithm was used to perform a 2D elastic reconstruction of a region with a depth range of 10 mm and a width range of 12 mm. Figures 7(a), 7(c), and 7(e) show the shear wave velocity image, elastic image, and ultrasonic elastic
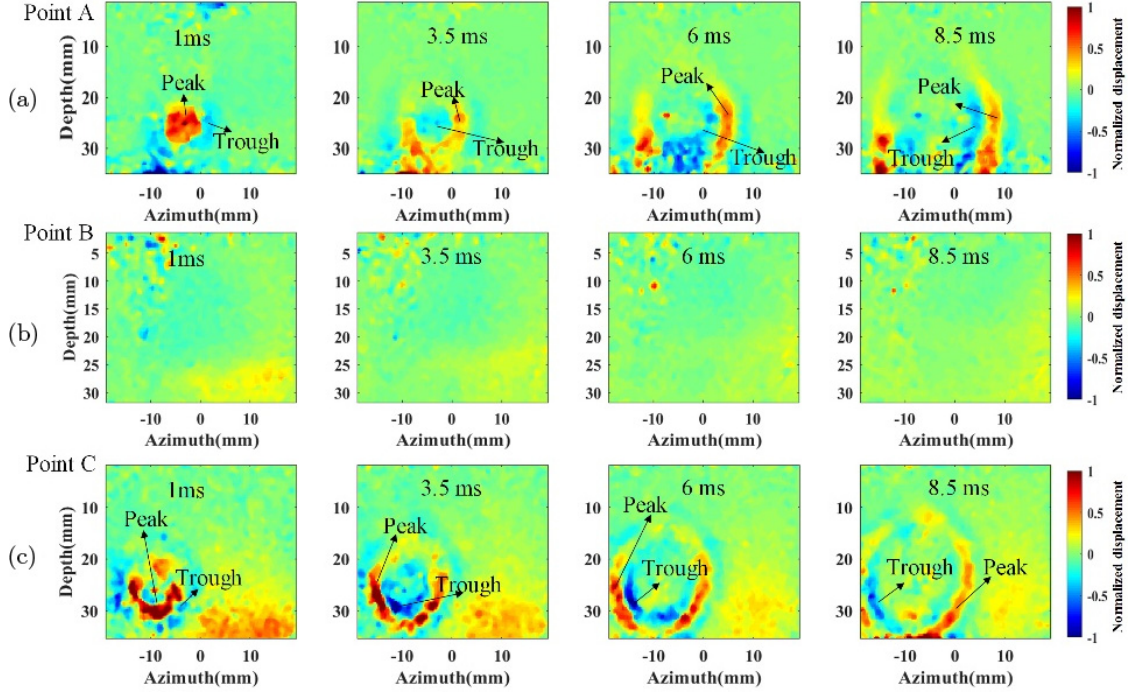
Fig. 4. Displacement maps. (a) Displacement maps of the experiment focusing on point A. (b) Displacement maps of the experiment focusing on point B. (c) Displacement maps of the experiment focusing on point C.

dual-modal image of the PASWE-reconstructed homogeneous phantom. This was compared with SSI results (Figs. 7(b), 7(d), and 7(f)). The 2Dshear wave velocity maps obtained by the two elastography methods were smooth and complete, and the wave velocity distribution was uniform. In addition, the wave velocity maps of the two have the same color under the same color bar, indicating that the shear wave speed of the two is similar. Elastography gives a better contrast to shear velocity imaging.

Young's modulus of the gelatin phantom can be calculated by $E = 0.0034C^{2.09}$ (C is the concentration of the gelatin solution in g/L).[32–34] Young's modulus reference value of the above homogeneous phantom is 82.04 kPa calculated by the formula. The shear wave velocity in the dotted box in Figs. 7(a) and 7(b) is averaged and Young's modulus is further obtained. They are compared to the

Fig. 5. Homogeneous phantom.

reference values and the results are shown in Table 1. The average shear wave velocity in the green dotted box of Fig. 7(a) is 5.20 m/s, and correspondingly, the data in Fig. 7(b) are 5.31 m/s. Their corresponding Young's modulus was derived to be 81.12 and 84.59 kPa, respectively. When their relative deviations from the reference value were compared, the PASWE result was closer to the reference value.

3.3. Heterogeneous phantom experiments

In order to further verify the feasibility and accuracy of PASWE, a heterogeneous phantom was made. Figure 8(a) shows a cylinder hard block with a diameter of 11 mm and a length of 14 mm that we made to mimic the tumor, composed of 8% gelatin and 12% graphite. The schematic diagram of the phantom is shown in Fig. 8(b), and the hard block was placed on a soft gelatin-based background consisting of 5% gelatin and 12% graphite.

Figure 9 (a) shows the ultrasound map of the phantom, with a, b, and c ROI marked by black boxes. Figures 9(b)9(d) show the spatial-temporal maps of shear wave propagation in regions a, b, and c, respectively. The dashed line represents the wave-
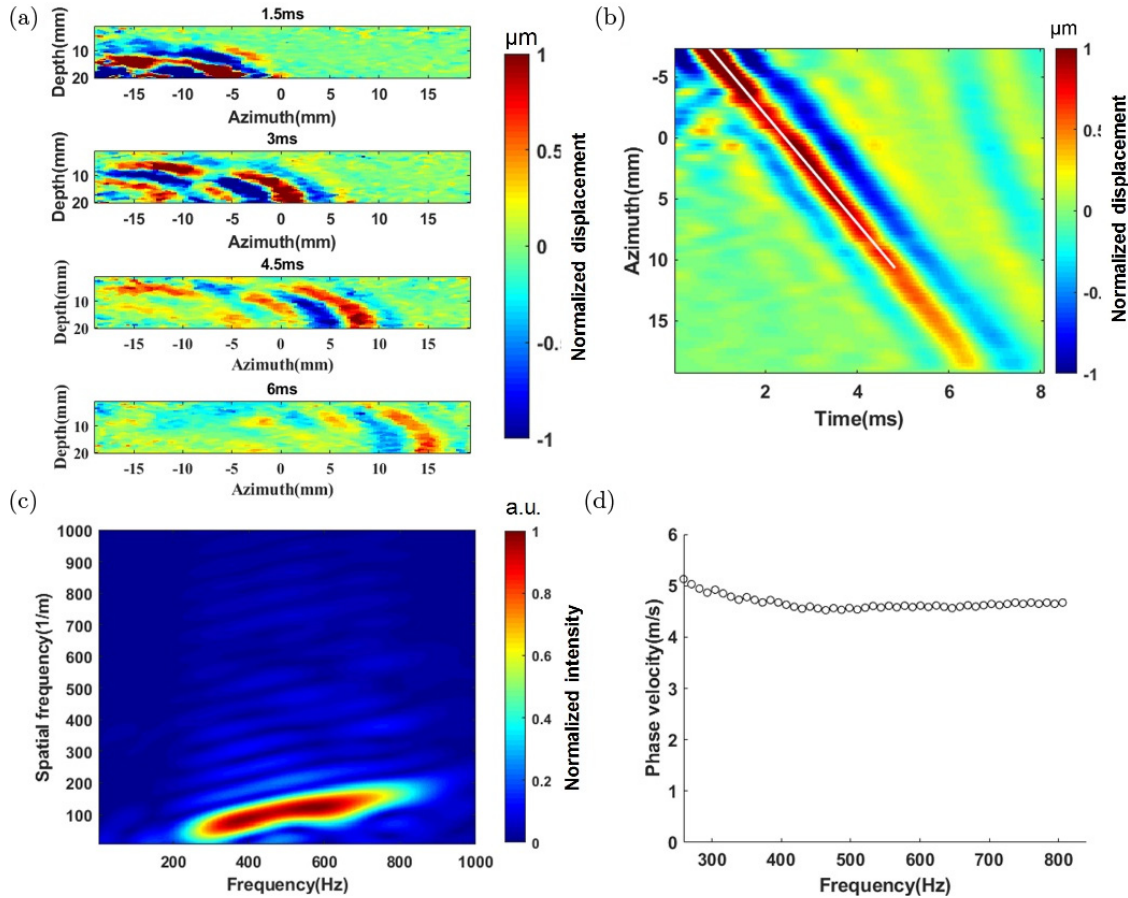
Fig. 6. The displacement variation, K-space displacement and phase velocity of shear wave (a) The displacement maps of 1.5, 3, 4.5, and 6 ms. (b) Spatial-temporal map of displacement, group velocity represented by a white line. (c) K-space normalized representation of z-axis displacement. (d) The relationship between phase velocity and temporal frequency.

front of the shear wave, and the slope of the dashed line represents the group velocity of the shear wave. The group velocities of shear waves in the three regions are 1.96, 3.89, and 2.01 m/s. Region b corresponds to the position of the hard block in the phantom, and its shear wave group velocity is faster than those in regions a and c, so region b is harder than regions a and c. The result is consistent with the hardness distribution of the phantom.

Figures 10(a) and 10(b) are ultrasound images obtained by SSI and PASWE, respectively. We compared PASWE with SSI by selecting six equidistant observation points on the left background and hard block, respectively, as shown in the red dots in the ultrasound images to analyze the changes of displacements with time. The time-displacement curves of SSI and PASWE are shown in Figs. 10(c) and 10(d), respectively. The arrows represent peaks of displacements. The peak time of the observation points in the hard block is denser

than that in the background, further showing that the shear wave propagates faster in the hard block, and the results of the two elastography methods are consistent. The arrival time of shear waves of each channel of the linear array transducer was plotted, and it was fitted in three segments, which were the background on the left, the hard block and the background on the right. The slope of the fitting curve represents the velocity of the shear waves. Figure 10(e) corresponds to the result of SSI, the shear waves velocity of the three sections is 2.2363, 3.6279, and 2.2719 m/s, respectively, while that of PASWE (Fig. 10(f)) are 1.9566, 3.8255, and 2.0107 m/s.

The resolution of the elastic image is related to the size of the sliding window selected when reconstructing the wave speed. To compare the experimental results of SSI and PASWE in terms of imaging resolution, the shear wave velocity of the heterogeneous phantom shown in Fig. 8 was
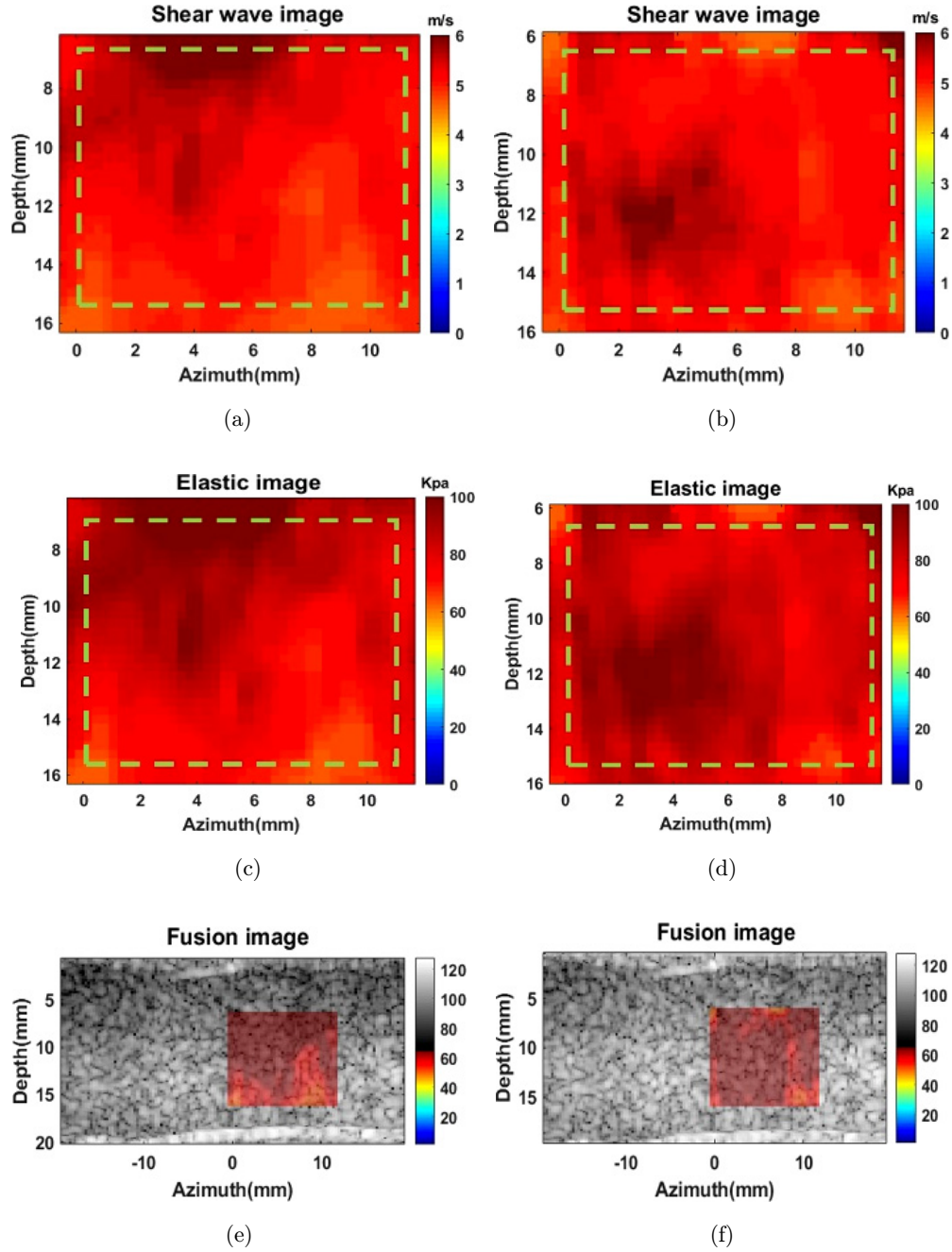
(a)

(b)

(c)

(d)

(e)

(f)

Fig. 7. Experimental results of the homogeneous phantom. (a), (c), and (e) are shear wave velocity images, elasticity images, and the ultrasonic/elastic dual-modal image obtained by PASWE. (b), (d), and (f) shear wave velocity image, elasticity image, and dual-modal ultrasonic/elastic image obtained by SSI.

Table 1.   Experimental results of homogeneous phantom.

Elastography methods	Average shear wave velocity (m/s)	Young's modulus (kPa)	Young's modulus reference (kPa)	Relative bias
PASWE	5.20	81.12	82.04	1.12%
SSI	5.31	84.59	82.04	3.11%

(a)

(b)
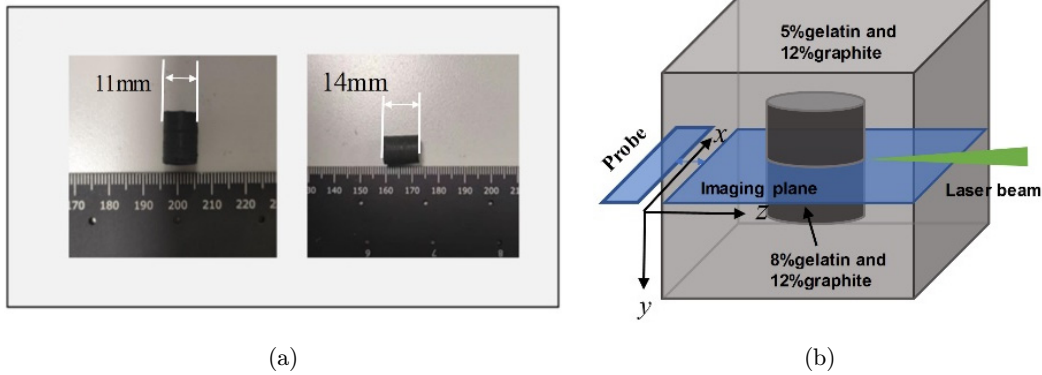
Fig. 8.   Heterogeneous phantom. (a) Cylinder hard block. (b) Schematic diagram of heterogeneous phantom.

reconstructed in 2D by using sliding windows of different sizes. Figure 11 shows the 2D reconstruction of the shear wave velocity of the heterogeneous phantom in SSI with sliding window size steps from 3×3 to 20×20 (each step represents 0.3 mm). Since only the shape of the contents and their elastic

properties with the background part are of interest, here, only the selected ROI is reconstructed. The results of the reconstruction of the sliding window with size steps 3×3, 6×6, and 20×20 in the figure cannot identify the boundary and shape of the contents. Although the image reconstructed by the
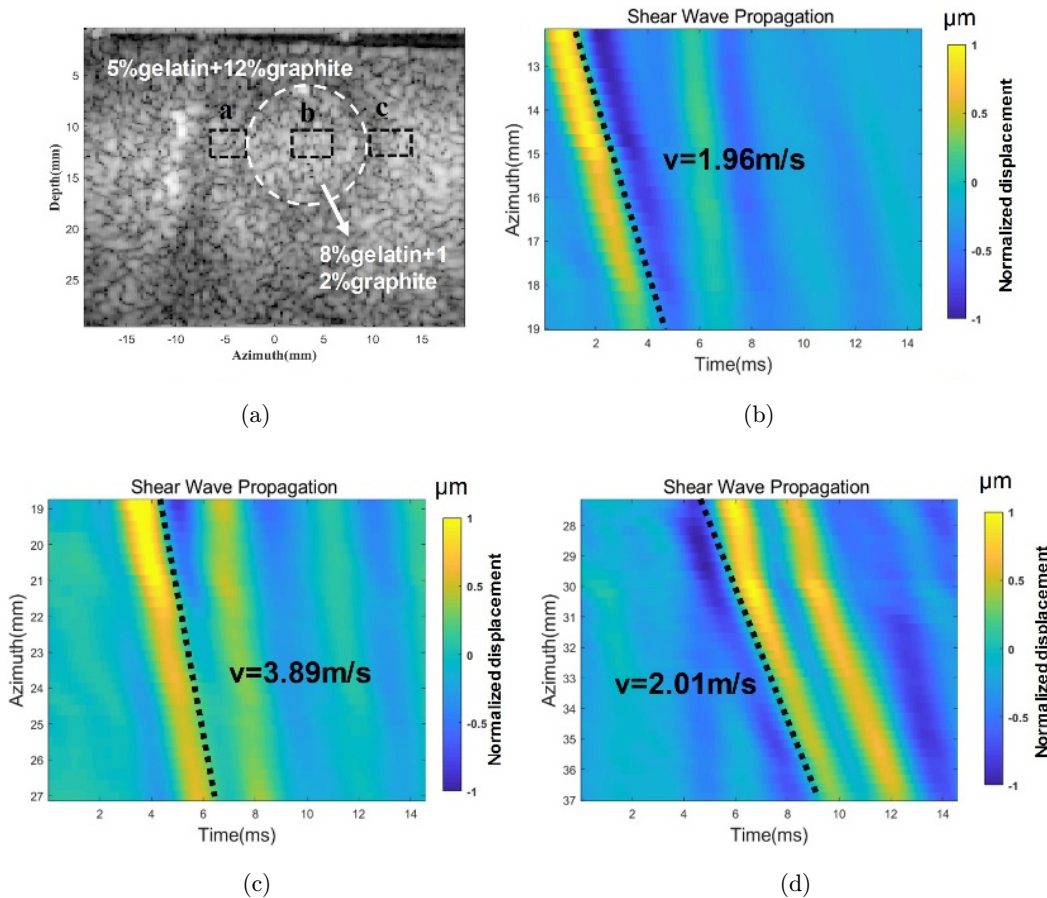

(a)

(b)

(c)

(d)

Fig. 9.   Spatial-temporal maps of shear wave propagation. (a) Phantom ultrasound image. (b) Spatial-temporal map of shear wave propagation in region a. (c) Spatial-temporal map of shear wave propagation in region b. (d) Spatial-temporal map of shear wave propagation in region c.
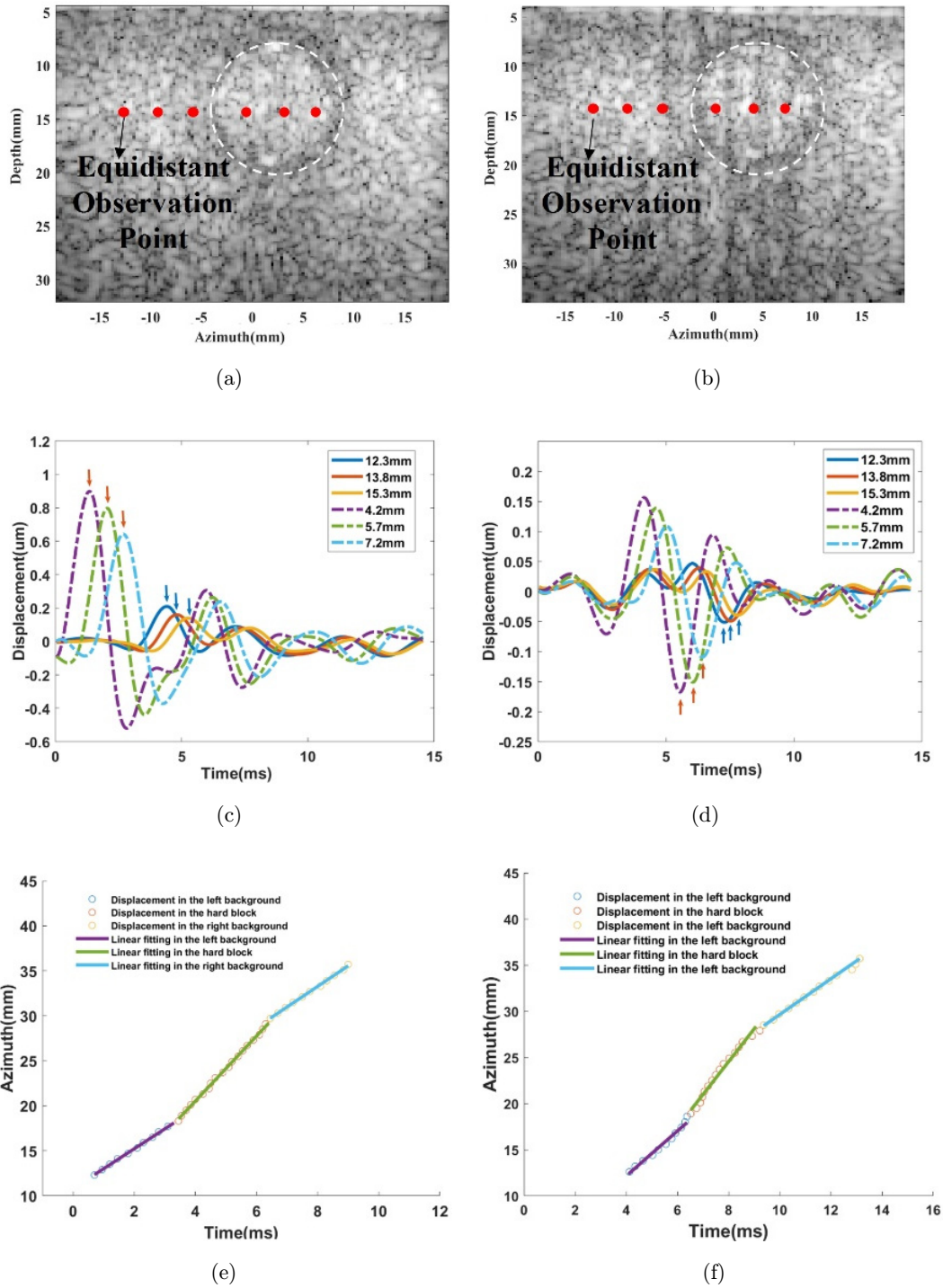
(a)

(b)

(c)

(d)

(e)

(f)

Fig. 10. Comparison of ultrasound images and time-displacement curves of SSI and PASWE. (a) Ultrasound image obtained by SSI. (b) Ultrasound image obtained by PASWE. (c) Time-displacement curves obtained by SSI. (d) Time-displacement curves obtained by PASWE. (e) The arrival time of the shear waves in the tissue of each channel and the fitting curves obtained by SSI. (f) The arrival time of shear waves in the tissue of each channel and the fitting curves obtained by PASWE.

sliding window with size steps 9×9 and 15×15 retains the shape of the hard block, there is a certain distortion and the accuracy of the reconstruction is low. According to the results of the study, a sliding window with a size step of 12×12 can reconstruct the shear wave velocity map with the best effect. Therefore, the block size that SSI can resolve is $3.6\,\text{mm} \times 3.6\,\text{mm}$.
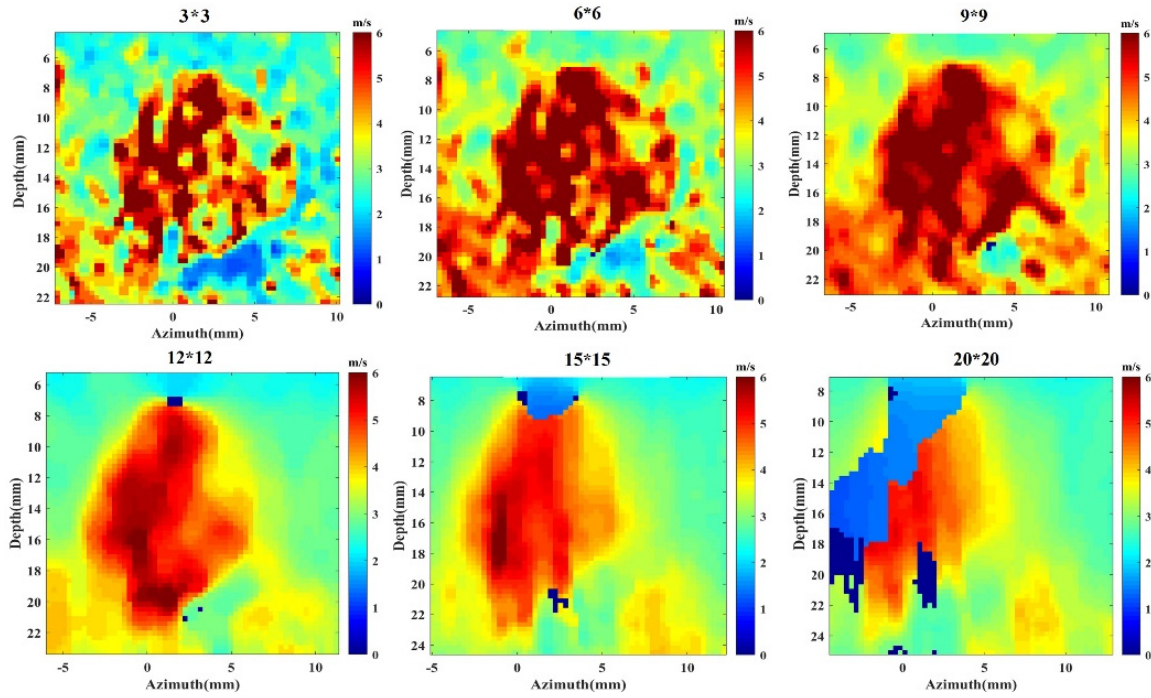
Fig. 11.   Results of the 2D wave velocity reconstruction of SSI using sliding windows of different step sizes.

Figure 12 shows the experimental results of the ultrasonic elasticity with the cylinder block Phantom. Figure 12(a) clearly shows the reddish part, corresponding to the location of the hard block. As shown in Figs. 12(b) and 12(c), the transverse diameter and the longitudinal diameter of the hard region in the velocity map are obtained by measuring the FWHM, which were 10.53 mm and 13.58 mm respectively. Compared with the actual diameter of 11 mm, the

transverse diameter is close to the actual size, and the longitudinal diameter error is larger.

Based on the SSI method, the average value of wave velocity data is calculated and compared with the reference value of wave velocity. The results are shown in Table 2. The SNR of the background and the content is 15.21 and 22.71, respectively, and the CNR of the elastic image is 18.56. The elastic modulus of the background and the content can be
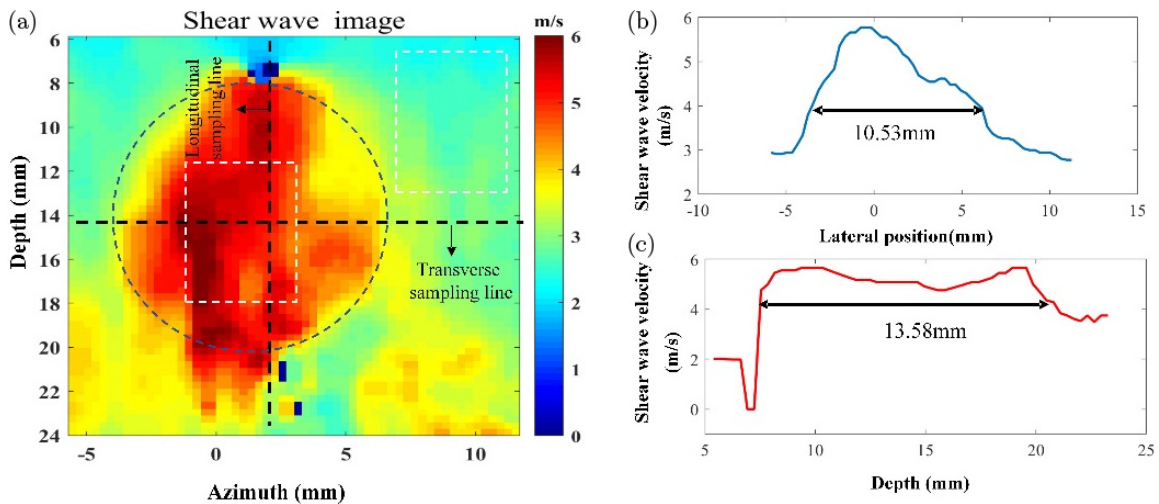

Fig. 12.   Experimental results comparison of SSI with cylinder block. (a) ROI shear waves velocity image obtained by SSI. (b) Lateral position sampling line velocity profile. (c) Longitudinal position sampling line velocity profile.

Table 2.   SSI methods experimental results of heterogeneous phantom.

SSI methods	Shear wave speed reference value (m/s)	Average wave speed of ROI (m/s)	Mean relative deviation	SNR	CNR
Background	2.43	2.72 ± 0.26	11.90%	15.21	18.56
Cylinder block	4.41	4.89 ± 0.61	10.89%	22.71	18.56

quantified accurately, but the ability to recover the longitudinal boundary is limited.

Figure 13 shows the 2D reconstruction of the shear wave velocity of the heterogeneous phantom in PASWE with sliding window size steps from 3 × 3 to 20 × 20. As the sliding window size step increases, the hard block boundary is smoother, and the wave velocity distribution is more uniform. However, if the size step is too large, such as 15 × 15 and 20 × 20, the accuracy of wave speed reconstruction will be reduced and the hard block boundary will be distorted to an increased degree. From the data studied, it can be seen that the sliding window obtained with a size step of 9 × 9 can provide the best elastic image. A well-defined circle can be seen in the elastic image, and it is clear that the hard block is harder than the surrounding part, which corresponds to the characteristics of the heterogeneous phantom. So, the block size that SSI can resolve is 2.7 mm × 2.7 mm. It can be seen that the resolution of PASWE in this experiment is higher than that of SSI.

Figure 14 shows a smooth and complete wave velocity map, the image center can be seen in a clear and complete circle, a more uniform distribution of wave velocity in the circle. From the data projection curves of the transverse and longitudinal sampling lines in the figure, it can be seen that the shear wave velocity in the hard part in the middle is more uniform, and the velocity transformation part is steeper than the corresponding data of the ultrasonic elasticity, indicating that its boundaries are clearer.   The   transverse   diameter   and   the
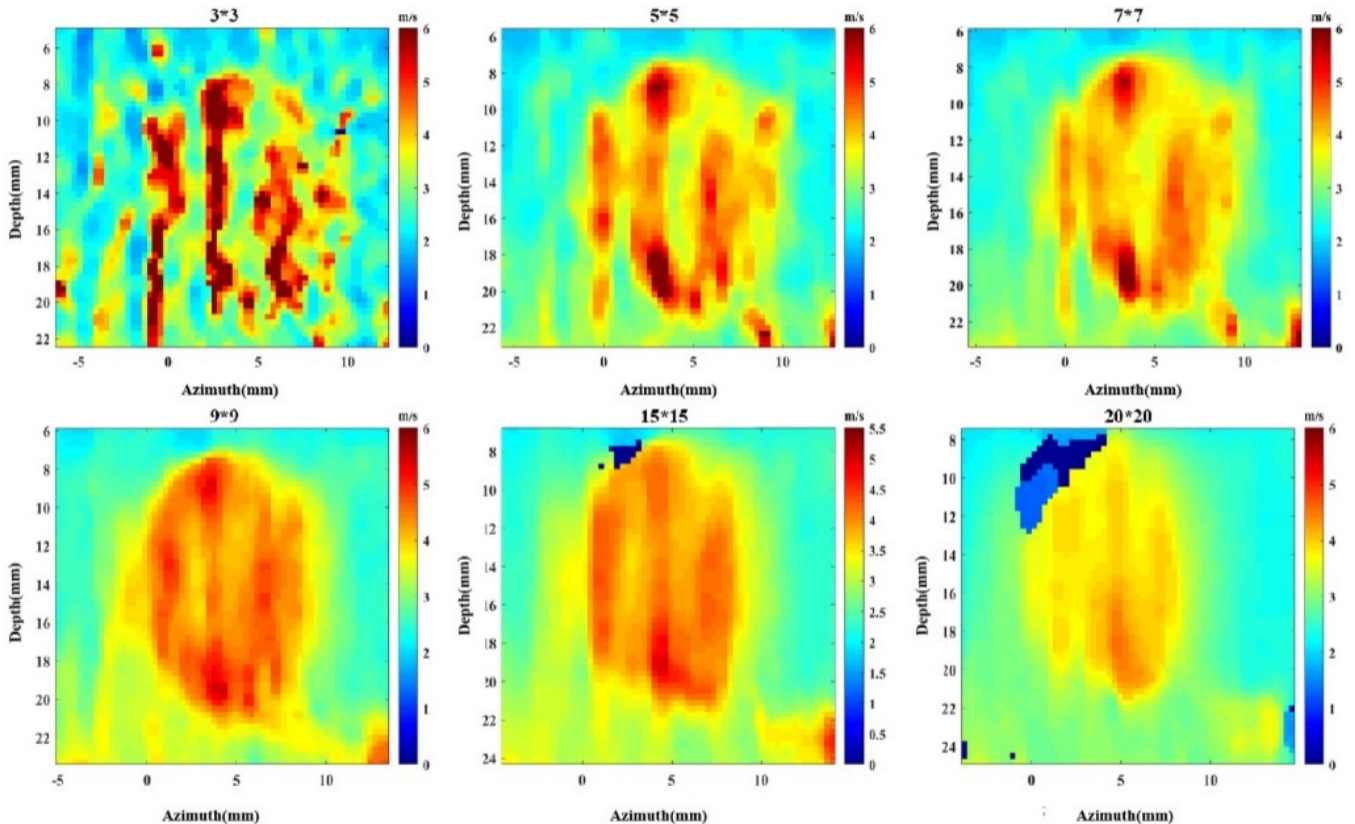

Fig. 13.   Results of the 2D wave velocity reconstruction of PASWE using sliding windows of different step sizes.
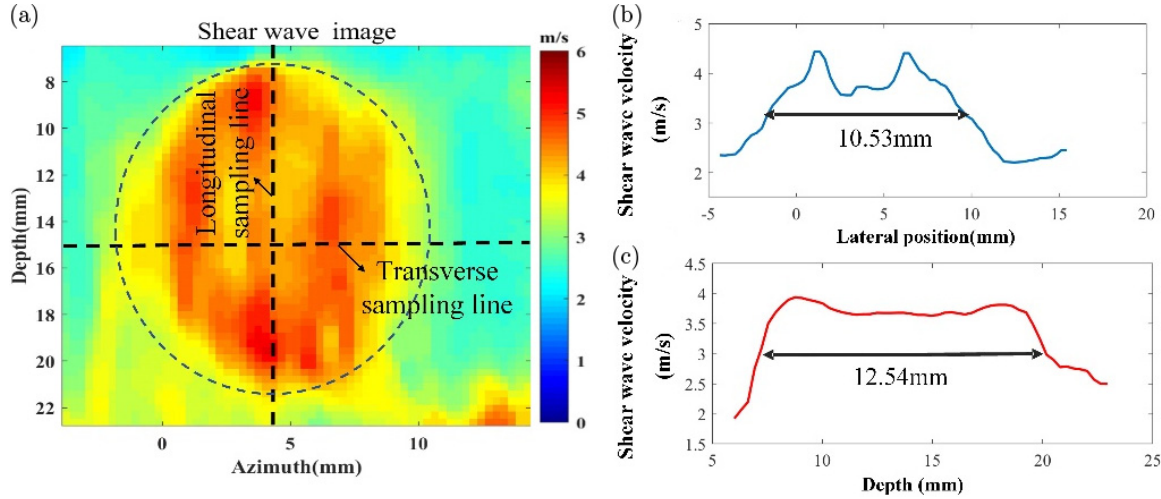
Fig. 14. Experimental results comparison of PASWE with cylinder block. (a) ROI shear waves velocity image obtained by PASWE. (b) Lateral position sampling line velocity profile. (c) Longitudinal position sampling line velocity profile.

longitudinal diameter of the block are 10.53 mm and 12.54 mm, respectively. The transverse diameter is very close to the actual diameter of the block (11 mm), and the estimation error of the longitudinal diameter is 1.54 mm.

Table 3 shows the results of averaging, SNR, and CNR data from heterogeneous phantom using the PASWE method. The relative deviation between the average value of ROI wave velocity and the reference value is less than 5%, which shows that the PA elastography function of the system can accurately estimate the elastic information of heterogeneous Phantom.

In the realization of PA elastography, the shear wave is first excited by laser focusing. Secondly, ultrasonic plane wave is used to track the amplitude and phase of shear wave, and the velocity of shear wave is obtained. Finally, the elastic modulus is derived.

Furthermore, the elastic images obtained by both will be analyzed. ROI was marked on the ultrasound image with an orange dashed box and the red dotted box corresponds to the position of the hard block (Fig. 15(a)). The elastic image reconstructed

from the best shear wave velocity map of PASWE is shown in Fig. 15(c).

A clear circle can be seen from the elastic image, with a clear boundary and a clear difference in hardness from the surrounding ground. The red area is harder than the surrounding blue part. By coordinate measurement, the lateral diameter of the hard block is 10.53 mm, and the longitudinal diameter is 12.10 mm, which is within 1.1 mm of the actual size of the hard block. Consequently, the ultrasound image and the elastic image of the SSI experiment are shown in Figs. 15(b) and 15(d). By comparison, the elastic images reconstructed by the two elastography methods are generally the same in hardness distribution, but the boundary reconstructed by PASWE has a better effect. To determine whether the red area in the elastic image matches the hard block in the ultrasound image, we put the reconstructed elastic images obtained by PASWE and SSI onto the ultrasound images to obtain dual-modal images of ultrasound and elasticity (Figs. 15(e) and 15(f)). The dual-modal imaging results show that the position of the hard block marked in the ultrasound images is covered by

Table 3. PASWE methods experimental results of heterogeneous phantom.

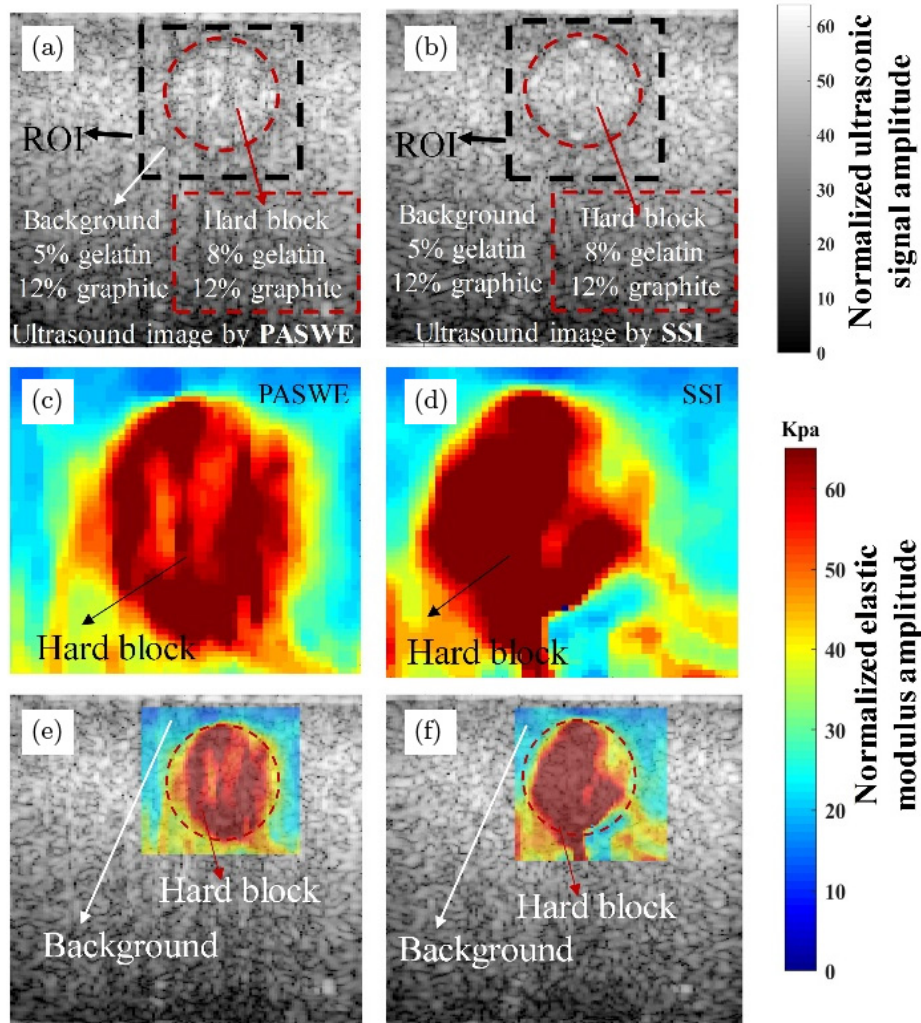| PASWE methods	Shear wave speed reference value (m/s)	Average wave speed of ROI (m/s)	Mean relative deviation	SNR	CNR
Background	2.43	2.33 ± 0.11	4.12%	62.67	24.80
Cylinder block	4.41	4.21 ± 0.22	4.54%	44.17	24.80

Fig. 15. PASWE of heterogeneous phantoms. (a) Phantom ultrasound image by PASWE. (b) Phantom ultrasound image by SSI. (c) Elasticity image of ROI obtained by PASWE. (d) Elasticity image of ROI obtained by SSI. (e) Phantom elasticity image obtained by PASWE on the ultrasound image. (f) Phantom elasticity image obtained by SSI on the ultrasound image.

the red area in the elastic images and their boundaries are basically consistent. The above results and the comparison with the SSI illustrate the ability of PASWE to reconstruct the elastic distribution of heterogeneous tissues and locate the tumor.

Table 4 shows the Young's modulus experimental results of homogeneous phantom. The average Young's modulus of hard block and surrounding background of PASWE are 59.94 and 16.95 kPa, respectively, and that of SSI are 52.53 and 18.79 kPa. It can be seen from the numerical values and images that the results of PASWE and SSI are very close, and both correspond to the hardness distribution of the actual phantom. The actual modulus of elasticity of hard block and background calculated is 51.46 and 17.84 kPa, respectively.[31]

Table 4. Young's modulus experimental results of homogeneous phantom.

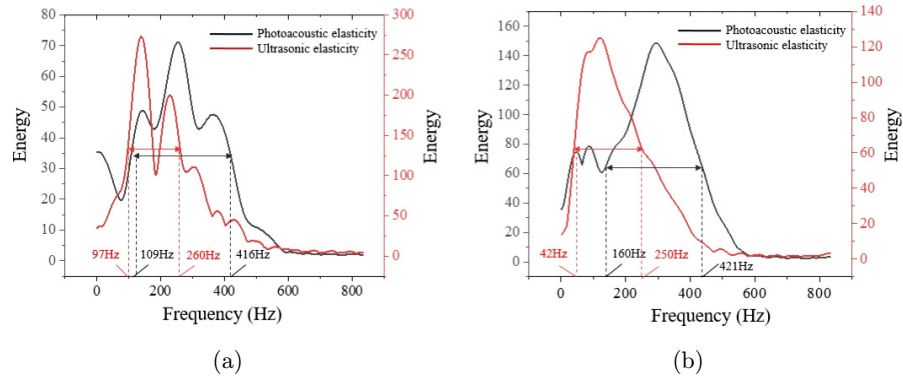| Elastography methods	Phantom type	Young's modulus (kPa)	Young's modulus reference (kPa)	Relative bias
PASWE	Cylinder block	50.94 ± 0.3	51.46	1.01%
SSI	Cylinder block	52.53 ± 0.21	51.46	2.08%
PASWE	Background	16.95 ± 0.14	17.84	4.99%
SSI	Background	18.79 ± 0.18	17.84	5.33%

Fig. 16. Comparison of the spatial shear wave energy peaks of SSI and PASWE. (a) Comparison of spatial shear wave energy peaks in hard block region. (b) Comparison of spatial shear wave energy peaks in the background region.

The PASWE and SSI results are similar to the actual Young's modulus of elasticity values and are within the allowable range of error. The ability of the PASWE method to quantify the elastic properties of the tissue was demonstrated. Here, it is worth noting that there is some difference in the elasticity images of PASWE and SSI, because the ARF pulse was focused from the same side of the ultrasonic transducer, while the laser was focused from the other side, resulting in differences in the propagation direction and propagation area of the shear waves.

The shear wave energy peaks of various frequencies in the shear wave K-space are plotted for the background region and the hard block region, and the results of the shear wave data comparison in the K-space are shown in Fig. 16. The black curve is the result of photoelasticity experiment, and the red curve is the result of ultrasonic elasticity experiment. The results show that the shear bandwidth of PASWE elastography is generally higher than that of SSI elastography by measuring the half-width. This improves the resolution and accuracy of elastography.

4. Discussion

Elastography can be used to diagnose the information of tissue hardness and to distinguish the changes of tissue pathophysiology.[4–6,35–37] PASWE holds promising for clinical usages. The tissue with light absorbers can be excited to produce shear waves, and the elastic distribution of the tissue can be reconstructed by tracing the propagation of shear waves. Based on PA effect, this method can produce shear wave with higher frequency and wider frequency band, and can realize high-resolution imaging. In this study, we demonstrated that laser can stimulate tissue with light absorption characteristics to generate thermal expansion to induce shear waves. We verified the feasibility of the method through experiments. By comparing the experimental results with SSI, it is verified that this method can perform quantitative elastic imaging on gelatin phantom. In addition, the frequency of the shear wave excited by the laser is higher than that excited by ARF, so higher spatial resolution can be obtained. Compared to traditional PA elastography, this method can obtain a larger imaging depth while ensuring imaging resolution, and the imaging quality is not greatly affected by the distribution of tissue light absorption characteristics. It has potential applications in clinical disease diagnosis requiring noncontact quantitative elasticity.

However, for complex biological tissues with complex absorption characteristics of absorbers, it is difficult to accurately distinguish different components in shear wave PA elastography excited by a single wavelength. Therefore, in future work, we will explore the diversity of elastic information in various complex biological tissue models and further optimize the PASWE reconstruction method, more accurate physiological information will be obtained by combining ultrasound/PA multimodal imaging.

5. Conclusions

Based on the linear-array PA system, in this paper, a new laser-excited SWE imaging method PASWE is proposed to reconstruct Young's modulus while combining PA technology with ultrafast ultrasound imaging. The proposed PASWE implements high-

frequency excitation of shear waves and noncontact elastic imaging. We use focused laser to excite shear wave and use ultrafast ultrasound imaging to track shear wave propagation. The Young's modulus of the tissue is reconstructed throughout the shear wave propagation region to further evaluate the elastic information of the tissue. We verified the feasibility of the method through experiments. By comparing the experimental results with SSI, it is verified that this method can perform quantitative elastic imaging on gelatin phantom. In addition, the frequency of the shear wave excited by the laser is higher than that excited by ARF, so higher spatial resolution can be obtained. Compared to traditional PA elastography, this method can obtain a larger imaging depth while ensuring imaging resolution, and the imaging quality is not greatly affected by the distribution of tissue light absorption characteristics. It has potential applications in clinical disease diagnosis requiring noncontact quantitative elasticity.

Acknowledgments

Conflict of Interest

The authors declare no conflict of interest.

ORCID

Yang Liu ⓘ https://orcid.org/0009-0003-5875-9781
Ruoyi Shi ⓘ https://orcid.org/0009-0009-2759-7090
Gang Li ⓘ https://orcid.org/0009-0009-6075-7914
Mingjian Sun ⓘ https://orcid.org/0000-0001-8719-524X

References

1. J.-L. Gennisson, T. Deffieux, M. Fink, M. Tanter, "Ultrasound elastography: Principles and techniques," *Diagn. Interv. Imaging* **94**, 487–495 (2013).
2. J. Ophir, S. K. Alam, B. S. Garra, F. Kallel, E. E. Konofagou, T. Krouskop, C. R. Merritt, R. Righetti, R. Souchon, S. Srinivasan, "Elastography: Imaging the elastic properties of soft tissues with ultrasound," *J. Med. Ultrason.* **29**, 155–171 (2002).
3. J. Ormachea, K. Parker, "Elastography imaging: The 30 year perspective," *Phys. Med. Biol.* **65**, 24TR06 (2020).
4. B. S. Garra, E. I. Cespedes, J. Ophir, S. R. Spratt, R. A. Zuurbier, C. M. Magnant, M. F. Pennanen, "Elastography of breast lesions: Initial clinical results," *Radiology* **202**, 79–86 (1997).
5. A. Sarvazyan, T. J. Hall, M. W Urban, M. Fatemi, S. R Aglyamov, B. S Garra, "An overview of elastography — an emerging branch of medical imaging," *Curr. Med. Imaging* **7**, 255–282 (2011).
6. G. Ferraioli, P. Parekh, A. B. Levitov, C. Filice, "Shear wave elastography for evaluation of liver fibrosis," *J. Ultrasound Med.* **33**, 197–203 (2014).
7. H. Li, G. Flé, M. Bhatt, Z. Qu, S. Ghazavi, L. Yazdani, G. Bosio, I. Rafati, G. Cloutier, "Viscoelasticity imaging of biological tissues and single cells using shear wave propagation," *Front. Phys.* **9**, 666192 (2021).
8. H. Xu, J.-Q. Mo, S. Chen, K.-N. An, Z.-P. Luo, "Elasticity measurements by shear wave elastography: Comparison and selection of shear wave, Rayleigh wave and lamb wave theory," *J. Mech. Med. Biol.* **18**, 1750119 (2018).
9. J. Bercoff, M. Tanter, M. Fink, "Supersonic shear imaging: A new technique for soft tissue elasticity mapping," *IEEE Trans. Sonics Ultrason.* **51**, 396–409 (2004).
10. L. Sandrin, B. Fourquet *et al.*, "Transient elastography: A new noninvasive method for assessment of hepatic fibrosis," *Ultrasound Med. Biol.* **29**, 1705–1713 (2003).
11. S. Das, A. Schill, C.-H. Liu, S. R. Aglyamov, K. V. Larin, "Laser-induced elastic wave classification: Thermoelastic versus ablative regimes for all-optical elastography applications," *J. Biomed. Opt.* **25**, 035004–035004 (2020).
12. L. Zhao, D. Vanderlaan, H. Yoon, J. Liu, C. Li, S. Y. Emelianov, "Ultrafast ultrasound imaging of surface acoustic waves induced by laser excitation compared with acoustic radiation force," *Opt. Lett.* **45**, 1810–1813 (2020).
13. M. Xu, L. V. Wang, "Photoacoustic imaging in biomedicine," *Rev. Sci. Instrum.* **77**, 041101 (2006).
14. M. S. Singh, A. Thomas, "Photoacoustic elastography imaging: A review," *J. Biomed. Opt.* **24**, 040902–040902 (2019).
15. Y. Shi, F. Yang, Q. Wang, "Photoacoustic viscoelasticity imaging dedicated to mechanical characterization of biological tissues," *J. Innov. Opt. Health Sci.* **10**, 1730005 (2017).
16. Y. Zhao, S. Yang, "Photoacoustic viscoelasticity imaging of biological tissues with intensity-

modulated continuous-wave laser," *J. Innov. Opt. Health Sci.* **6**, 1350033 (2013).

17. M. Ishihara, M. Sato, S. Sato, T. Kikuchi, K. Fujikawa, M. Kikuchi, "Viscoelastic characterization of biological tissue by photoacoustic measurement," *Jpn. J. Appl. Phys.* **42**, L556 (2003).

18. G. Gao, S. Yang, D. Xing, "Viscoelasticity imaging of biological tissues with phase-resolved photoacoustic measurement," *Opt. Lett.* **36**, 3341–3343 (2011).

19. P. Hai, J. Yao, G. Li, C. Li, L. V. Wang, "Photoacoustic elastography," *Opt. Lett.* **41**, 725–728 (2016).

20. P. Hai, Y. Zhou, L. Gong, L. V. Wang, "Quantitative photoacoustic elastography in humans," *J. Biomed. Opt.* **21**, 066011–06011 (2016).

21. J. P. Monchalin, "Laser-ultrasonics: Principles and industrial applications," *Ultrasonic and Advanced Methods for Nondestructive Testing and Material Characterization*, pp. 70–115 (2007).

22. P. Grasland-Mongrain, Y. Lu, F. Lesage, S. Catheline, G. Cloutier, "Generation of shear waves by laser in soft media in the ablative and thermoelastic regimes," *Appl. Phys. Lett.* **109**, 221901 (2016).

23. R. M. White, "Generation of elastic waves by transient surface heating," *J. Appl. Phys.* **34**, 3559 (1963).

24. L. E. Drain, *Laser Ultrasonics: Techniques and Applications*, Routledge (2019).

25. M. L. Palmeri, M. H. Wang, J. J. Dahl, K. D. Frinkley, K. R. Nightingale, "Quantifying hepatic shear modulus in vivo using acoustic radiation force," *Ultrasound Med. Biol.* **34**, 546–558 (2008).

26. P. Song, H. Zhao, A. Manduca, M. W. Urban, J. F. Greenleaf, S. Chen, "Comb-push ultrasound shear elastography (CUSE): A novel method for two-dimensional shear elasticity imaging of soft tissues," *IEEE Trans. Med Imaging* **31**, 1821–1832 (2012).

27. D. C. Mellema, P. Song, R. R. Kinnick, M. W. Urban, J. F. Greenleaf, A. Manduca, S. Chen, "Probe oscillation shear elastography (PROSE): A

28. C. Kasai, K. Namekawa, A. Koyano, R. Omoto, "Real-time two-dimensional blood flow imaging using an autocorrelation technique," *IEEE Trans. Ultrason. Ferroelectr. Freq. Control* **32**, 458–464 (1985).

29. A. Manduca *et al.*, "Spatio-temporal directional filtering for improved inversion of MR elastography images," *Med. Image Anal.* **7**, 465–473 (2003).

30. T. Deffieux, J. Gennisson, J. Bercoff *et al.*, "On the effects of reflected waves in transient shear wave elastography," *IEEE Trans. Ultrason. Ferroelectr. Freq. Control* **58**, 2032–2035 (2011).

31. N. C. Rouze, M. H. Wang, M. L. Palmeri, K. R. Nightingale, "Robust estimation of time-of-flight shear wave speed using a radon sum transformation," *IEEE Trans. Ultrason. Ferroelectr. Freq. Control* **57**, 2662–2670 (2010).

32. T. J. Hall, M. Bilgen, M. F. Insana, T. A. Krouskop, "Phantom materials for elastography," *IEEE Trans. Ultrason. Ferroelectr. Freq. Control* **44**, 1355–1365 (1997).

33. Z. Dong *et al.*, "Three-dimensional shear wave elastography using a 2D row column addressing (RCA) array," *BME Front.* **2022**, 9879632 (2022).

34. B. Z. Fite *et al.*, "A review of imaging methods to assess ultrasound-mediated ablation," *BME Front.* **2022**, 9758652 (2022).

35. M. S. Singh, H. Jiang, "Ultrasound (US) transducer of higher operating frequency detects photoacoustic (PA) signals due to the contrast in elastic property," *AIP Adv.* **6**, 025210 (2016).

36. M. S. Singh, H. Jiang, "Elastic property attributes to photoacoustic signals: An experimental phantom study," *Opt. Lett.* **39**, 3970–3973 (2014).

37. M. S. Singh, S. Paul, A. Thomas, "Fundamentals of photoacoustic imaging: A theoretical tutorial," *LED-Based Photoacoustic Imaging: From Bench to Bedside*, Vol. 3, p. 21. Springer Singapore, Singapore (2020).